Nonlinear precipitation response to El Niño and global warming in the Indo-Pacific

Christine T. Y. Chung · Scott B. Power ·
Julie M. Arblaster · Harun A. Rashid ·
Gregory L. Roff

Abstract Precipitation changes over the Indo-Pacific during El Niño events are studied using an Atmospheric General Circulation Model forced with sea-surface temperature (SST) anomalies and changes in atmospheric CO_2 concentrations. Linear increases in the amplitude of the El Niño SST anomaly pattern trigger nonlinear changes in precipitation amounts, resulting in shifts in the location and orientation of the Intertropical Convergence Zone (ITCZ) and the South Pacific Convergence Zone (SPCZ). In particular, the maximum precipitation anomaly along the ITCZ and SPCZ shifts eastwards, the ITCZ shifts south towards the equator, and the SPCZ becomes more zonal. Precipitation in the equatorial Pacific also increases nonlinearly. The effect of increasing CO_2 levels and warming SSTs is also investigated. Global warming generally enhances the tropical Pacific precipitation response to El Niño. The precipitation response to El Niño is found to be dominated by changes in the atmospheric mean circulation dynamics, whereas the response to global warming is a balance between dynamic and thermodynamic changes. While the dependence of projected climate change impacts on seasonal variability is well-established, this study reveals that the impact of global warming on Pacific precipitation also depends strongly on the magnitude of the El Niño event. The magnitude and structure of the precipitation changes are also sensitive to the spatial structure of the global warming SST pattern.

1 Introduction

The El Niño Southern Oscillation (ENSO) is the main driver of internal climate variability in the Pacific (Philander 1990; Australian Bureau of Meteorology and CSIRO 2011). El Niño (EN) events are typically characterised by a warming of the equatorial central-eastern Pacific sea-surface temperatures (SSTs) whereas La Niña (LN) events are, roughly speaking, the reverse of this (e.g. Bradley et al. 1987; Ropelewski and Halpert 1989). Two major precipitation features in the tropical Pacific which are affected by ENSO variability are the Intertropical Convergence Zone (ITCZ; e.g. Waliser and Gautier 1993; Chiang et al. 2000; Münnich and Neelin 2005) and South Pacific Convergence Zone (SPCZ; e.g. Streten 1973; Trenberth 1976; Meehl 1987; Vincent 1994; Folland et al. 2002; Vincent et al. 2011; Widlansky et al. 2011; Brown et al. 2011; Australian Bureau of Meteorology and CSIRO 2011), shown in Fig. 1a. The ITCZ is a band that stretches across the Pacific, just north of the equator. The SPCZ intensifies annually between November–April and extends south east from the western central Pacific to approximately 30°S, 240°E. During El Niño years, there is generally increased precipitation over the central-eastern Pacific, and decreased precipitation along the south west of the SPCZ. Figure 1b shows the precipitation anomalies associated with El Niño years between 1979 and 2009. Figure 1c, d show, respectively, the precipitation bias from our Atmospheric General Circulation Model's (AGCM) simulated climatology and the composite El Niño

C. T. Y. Chung (✉) · S. B. Power · J. M. Arblaster · G. L. Roff
Centre for Australian Weather and Climate Research, Bureau of Meteorology, GPO Box 1289, Melbourne, VIC, Australia
e-mail: c.chung@bom.gov.au

H. A. Rashid
Centre for Australian Weather and Climate Research, CSIRO Marine and Atmospheric Research, Aspendale, VIC, Australia
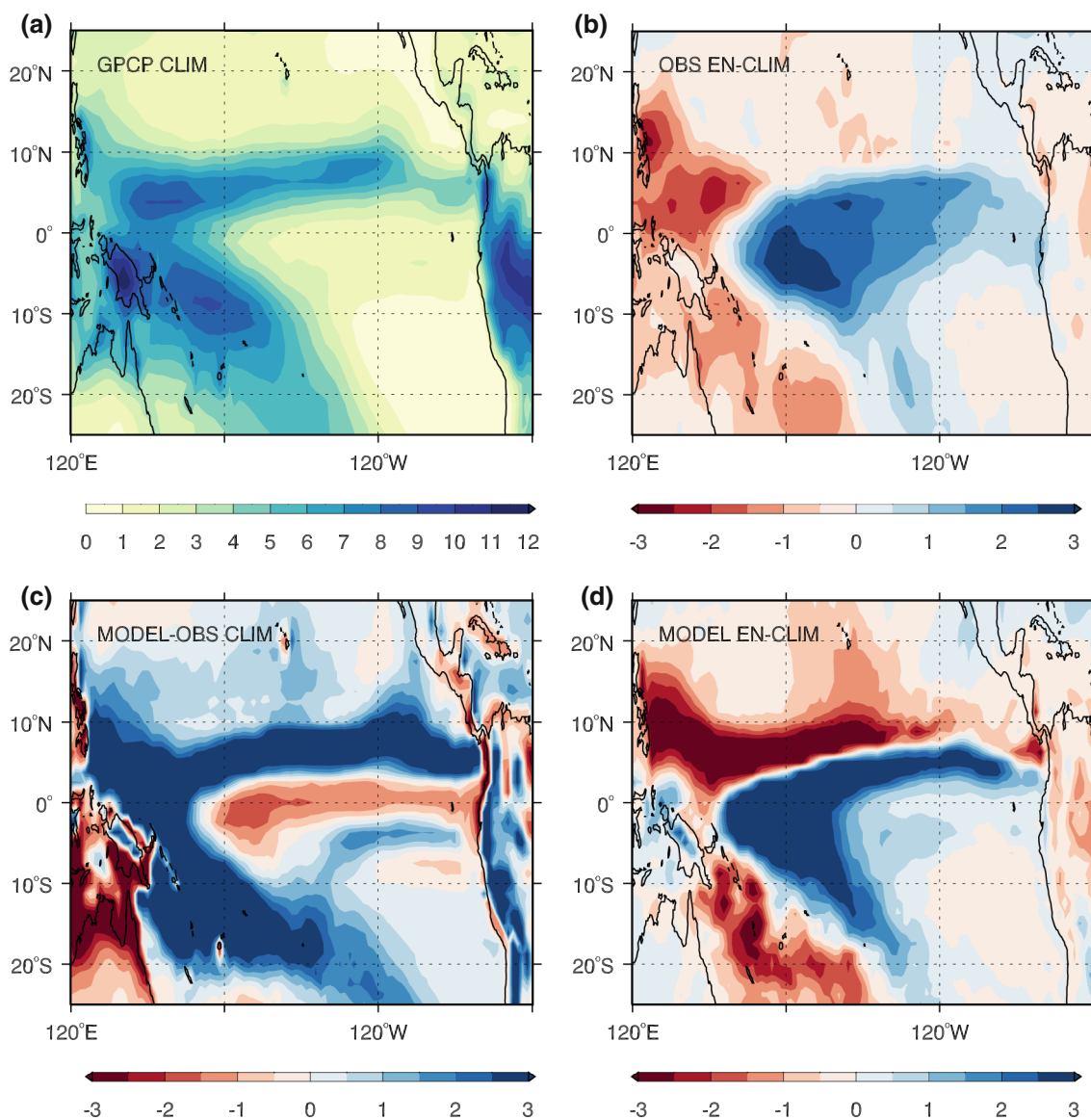
Fig. 1 Top panels GPCP observations of precipitation (November 1979–April 2009) showing **a** the mean November–April positions of the ITCZ and SPCZ for all years and **b** anomalies associated with El Niño years. Bottom panels **c** Biases in the ACCESS AGCM simulated precipitation climatology, and **d** the simulated precipitation anomalies for El Niño years. Units are mm/day

anomalies from the AGCM. These are discussed in detail in Sect. 2.

There is little consensus from models on how ENSO variability is going to change in future climate (Meehl et al. 2007; Vecchi and Wittenberg 2010; Collins et al. 2010; Australian Bureau of Meteorology and CSIRO 2011). Some models show an increase in SST variability, some a decrease and some show little if any change (Meehl et al. 2007). In contrast, a more recent study into the ENSO-driven precipitation minus evaporation (P − E) changes between the twentieth and twentyfirst centuries in CMIP3 models suggests that ENSO-driven P − E variability is projected to increase (Seager et al. 2012). Under

El Niño conditions, P − E across the equatorial Pacific is projected to increase, while precipitation in the south west Pacific is projected to decrease (Seager et al. 2012). This highlights the possibility that there might be robust changes in ENSO-driven precipitation changes even if there are not in SST or mean sea level pressure (Cai et al. 2012). More specifically, studies of the impact of global warming on the SPCZ in the CMIP3 models find that during El Niño years, the slope of the SPCZ decreases, and it shifts towards the equator (Brown et al. 2012a). However, it is noted that most models simulate an SPCZ that is too zonal and so projections of the SPCZ are somewhat uncertain (Brown et al. 2012a). Widlansky et al. (2013) identified

two competing mechanisms which contribute to the uncertainty in SPCZ projections in CMIP3 and CMIP5 models: the "wet gets wetter" (thermodynamic) and "warmest gets wetter" (dynamic) responses. Using a hierarchy of models to remove SST biases common in coupled models, the authors estimate a drying of the SPCZ for moderate tropical warming (1 − 2 °C), and a wetter SPCZ for stronger tropical warming (>3 °C).

Previous research has shown that El Niño and La Niña are in fact not simply equal and opposite, but can trigger nonlinear global responses in e.g. precipitation, sea level pressure (SLP), and winds (Mullan 1996; Hoerling et al. 1997, 2001; Monahan and Dai 2004; Power et al. 2006). For example, the SLP response to ENSO is more linear in the tropics, but nonlinear in the extratropics (Lau and Boyle 1987; Mullan 1996; Hoerling et al. 1997). In Australia, the precipitation response during La Niña is stronger than during El Niño, although this relationship is affected by multidecadal variability (Power et al. 2006; Cai et al. 2010). Additionally, El Niño events tend to decay more rapidly than La Niña events, possibly due to an imbalance in surface wind anomalies over the western Pacific (Okumura and Deser 2010), asymmetric wind-stress responses to changes in the SST (Ohba and Ueda 2009), a combination of asymmetric SST anomalies and anomalous heating in the western Pacific (Wu et al. 2010), or asymmetries in the meridional wind movements (McGregor et al. 2012, 2013).

It has also been noted that nonlinearities in the responses to ENSO variability are more apparent in strong El Niño events, when the SST anomalies are >2 standard deviations of the interannual variability (Hoerling et al. 2001). Previously, Hoerling et al. (2001) (hereafter HKX01) investigated the nonlinearity between El Niño and La Niña by performing idealized Atmospheric General Circulation Model (AGCM) experiments. They forced their model with tropical Pacific SSTs from 1963 to 1989 projected onto the first EOF of SSTs from 1948 to 1999. "Warm" (El Niño) and "cold" (La Niña) events were identified, and separate composites were created for "weak" (0.5–1.0 standardized departures of the first EOF index) and "strong" (2–3 standardized departures of the first EOF index) anomalies. They found that the changes in tropical precipitation between weak and strong El Niño composites were larger and more widespread than for the La Niña composites. Observations show that very strong El Niño events (e.g. 82/83 and 97/98) trigger a different precipitation response to that of moderate El Niño events (Vincent et al. 2011). In particular, the SPCZ obtains a zonal orientation, and merges with the ITCZ. Recent research suggests that the frequency of zonal SPCZ events might increase under global warming (Cai et al. 2012).

Some of the non-linear response of precipitation to SST anomalies linked to ENSO can arise because atmospheric convection can sometimes be linked to the position of local maxima in SST, rather than to SST anomalies directly (Hoerling et al. 1997). Thus a non-uniform SST anomaly can shift the position of maximum SST, sometimes causing a shift in the position of deep convection in the overlying atmosphere. This is known to occur during El Niño events (Hoerling et al. 1997).

In this paper, we focus on the precipitation response to El Niño events. Instead of classifying individual observed El Niño events, we create a composite of SST anomalies from all El Niño events from November 1979 to April 2009, and systematically increase this anomaly without changing its spatial structure. El Niño events are sometimes classified into, for example, "warm pool/central Pacific" (WP/CP) and "cold tongue/eastern Pacific" (CT/EP) events (e.g. Kug et al. 2009; Yeh et al. 2009) which have quite distinct SST anomalies. Observations show that since the late 1990s, there has been a tendency towards WP/CP SST anomalies (Kug et al. 2009; Yeh et al. 2009), however there is still uncertainty as to whether this is due to global warming or natural multidecadal variability (Newman et al. 2011; McPhaden et al. 2011). Therefore as the El Niño SST anomaly used here is based on a composite of El Niño events, it includes both classes of events. This allows us to study how increasing only the amplitude, not the structure, of El Niño SST anomaly affects the precipitation response.

It is possible that this nonlinear behaviour will change under global warming. To test this hypothesis we extend the work of HKX01 by forcing the AGCM using SST changes linked to *both* El Niño *and* global warming, as well as changes to atmospheric concentrations of greenhouse and other gases. The global warming SST pattern is estimated using the Multi-Model Ensemble Mean (MMEM) SST warming projected by CMIP3 models under the Special Report on Emissions Scenarios (SRES) A2 scenario (Meehl et al. 2007) and by increasing atmospheric CO_2 concentrations. We exploit the absence of a consensus on changes to the spatial structure of El Niño SST anomalies under global warming and assume that no changes occur. We use a single composite El Niño pattern based on observations, but multiply this pattern by numbers ranging from 0 (no El Niño) through to 4.0 (a very large El Niño event). The AGCM response is determined in the presence or absence of the changes associated with global warming. We focus on the response of precipitation over the Indo-Pacific Ocean during El Niño and neutral years only. We find that there are indeed important robust differences in the nonlinear precipitation response during El Niño in the twentyfirst century, even if the spatial structure of El Niño SST anomalies do not change.

This paper is structured as follows. The AGCM is described in Sect. 2. The SST-forced experiments are

detailed in Sect. 3. In Sect. 4, we describe the effects of increasing the magnitude of the El Niño anomalies on tropical precipitation, focusing on the nonlinearity that arises in the Indo-Pacific region. We then describe the impact of adding the global warming signal to the El Niño anomaly in Sect. 5. In Sect. 6, we highlight the nonlinear precipitation response in several key regions, including the ITCZ and SPCZ. We summarise our key findings and discuss our results in Sect. 7.

2 Atmospheric model description

For these experiments, we use the Australian Community Climate and Earth-System Simulator (ACCESS) AGCM. The AGCM has a non-hydrostatic dynamical core and is based on a version of the UK Met Office Unified Model (Davies et al. 2005; Martin et al. 2010). The model uses Semi-Lagrangian advection dynamics with semi-implicit time integration (Staniforth et al. 2003; Davies et al. 2005). The AGCM was configured to have the HadGEM2 (revision 1.0) climate configuration (Martin et al. 2010, 2011) that incorporates sophisticated parameterisations of unresolved physical processes, including those for the boundary layer, convection, clouds, radiation, aerosols, land surface, gravity-wave drag, and hydrological cycle. The AGCM is a grid-point model with a height-based, terrain-following vertical coordinate. We use the N96 horizontal resolution, equivalent to $1.25° \times 1.875°$ in latitude and longitude, and 38 vertical levels, with the model top placed at ~ 39 km.

The physical processes in the HadGEM2 family of models are described in detail in Martin et al. (2011). There have been many model improvements over the previous version, HadGEM1 (Martin et al. 2006), leading to substantial performance improvements for the Had-GEM2 models. Most importantly, changes were made to the convection scheme to improve simulations of the diabatic heating profile in the tropics, and to the land surface scheme to reduce the warm bias over Northern Hemisphere continents Martin et al. (2011). The model uses the general 2-stream Edwards–Slingo radiative transfer scheme to parameterise the longwave and shortwave radiation processes (Edwards and Slingo 1996). The boundary layer processes are parameterised using a non-local mixing scheme for unstable layers (Lock et al. 2000) and a local Richardson number scheme for stable layers (Smith 1990, 1993).

The model uses the Gregory–Rowntree mass flux convection scheme with an adaptive detrainment parameterization for deep and mid convection (Gregory and Rowntree 1990; Gregory et al. 1999). It uses the CAPE closure scheme to calculate the cloud base mass flux (Fritsch and Chappell 1980). Cloud formation is modelled using a

symmetric triangular probability distribution of total moisture and a temperature variable (Smith 1990), using the parametrization for the critical relative humidity function of Cusack et al. (1999) that determines the width of the probability distribution. The large-scale precipitation is modelled using an improved version of the mixed phase microphysics scheme of Wilson and Ballard (1999).

The MOSES-II land surface scheme is used, which calculates the surface energy balance for nine different surface types (Essery et al. 2001) and has four soil moisture levels. Aerosols are held constant and natural forcing (from solar variability and volcanic eruptions) is ignored.

Note that there are some important differences between this developmental version of the ACCESS AGCM and the final version (HadGEM2 revision r1.1) used for CMIP5 simulations (Bi et al. 2012). These differences, detailed in Martin et al. (2011), include the absence in the developmental version of time-varying natural forcings arising from the solar output variability and volcanic eruptions. However, the natural forcings were not required for the experiments described in this paper.

Figure 1c shows the climatological precipitation from the model and can be compared directly to the observations (Fig. 1a) to provide an indication of how well the model performs. The model reproduces the structure of the ITCZ and SPCZ reasonably well: the model ITCZ is accurately positioned between 0° and 10°N, and the SPCZ is diagonally oriented. However, the model uniformly overestimates the precipitation in these bands by ~ 5–6 mm/day compared with the observations. The wet regions of western South America and central Africa are reproduced, though precipitation over the Indonesian archipelago, Papua New Guinea, and north Australia is generally underestimated. To evaluate how well the model reproduces the precipitation response to EN, Fig. 1d shows the precipitation anomalies for $\alpha = 1$. This can be compared to Fig. 1b, which shows observed precipitation for all EN years within the observation period. The locations of the wet and dry regions over the equatorial Pacific are well-reproduced, although the model overestimates the wet anomaly over the central Pacific by ~ 4–5 mm/day. The general overestimation of precipitation over the ITCZ and SPCZ in AMIP experiments is a common feature in many models (Widlansky et al. 2013). Nevertheless the location of all major precipitation features and anomalies are reproduced well, and the model precipitation is deemed sufficiently accurate to use for the experiments conducted.

3 SST experiments

We force the model with annually-repeating monthly-mean climatological SSTs and sea ice derived from the Hurrell

Table 1 List of El Niño years between 1979 and 2009 used to create the composite for the AGCM experiments

El Niño years 1979–2009
1982
1987
1991
1992
1993
1994
1997
2002
2006

et al. (2008) dataset.[1] Only years for which GPCP precipitation data was available are used (i.e. 1979–2009; Adler et al. 2003; Huffman et al. 2009). For each experiment, the model is run for 20 years and the first 5 years are discarded. We perform two sets of experiments, varying one component of the model each time, as detailed below.

Each set comprises five members, which we label 0–4. Member 0 represents the 'control' run, using just climatological SSTs (with or without an additional global warming SST pattern). We then create a global composite of the El Niño SST anomalies (monthly means from November to April) from November 1979 to April 2009 and add multiples of this to the SST climatology for the next four members ([1–4]). For the sake of clarity, the El Niño anomaly multiplication factor is called α, an integer that ranges between 0 and 4 in these experiments. The El Niño SST composite (which we will refer to as $SSTA_{EN}$) was calculated using the averages of the years in Table 1. In these years the Southern Oscillation Index (SOI) averaged over the period June–December was less than −5 (for reference, the average 1979–2009 SOI is −2.0). This simple objective method was used previously to identify El Niño years (Power et al. 2006; Power and Smith 2007). The $SSTA_{EN}$ (November–April) is plotted in Fig. 2. It shows a warm anomaly across the eastern equatorial Pacific bounded on the north- and south west by a cold anomaly. Figure 2 shows a spatial structure similar to that of the first SST EOF in the experiments of HKX01 (cf. their Fig. 1b).

To put $SSTA_{EN}$ into context, the average November–April NINO3 indices (monthly SST anomalies averaged between 210°E–270°E, 5°S–5°N) for $1 \leq \alpha \leq 4$ are 1.22, 2.13, 3.03, and 3.93 respectively (approximately 0.9, 1.6, 2.3, and 3.0 times the standard deviation of the monthly 1979–2009 NINO3 indices respectively). The 1982/1983 El Niño event had an average November–April NINO3

index of 2.72, peaking at 3.19 in March 1983, whereas the 1997/1998 El Niño event had an average November–April NINO3 index of 2.96, peaking at 3.24 in March 1998. We note, however, that the $\alpha = 3,4$ cases are not directly comparable to the 1982/1983 and 1997/1998 events, as the spatial structure of the SST anomalies during those years differ from the composite $SSTA_{EN}$ pattern.

The first set of experiments (labelled 20C_[0EN–4EN]) represents the present climate. Its first member (20C_0EN) is the control run, in which we use only climatological SSTs and the average of observed 1958–2008 Mauna Loa CO_2 levels (346 ppm). The CO_2 levels are kept constant throughout the runs. The second set (labelled 21C_[0EN–4EN]) has the same input, except we add an additional global warming SST pattern (ΔSST_{GW}) to the SSTs and increase the CO_2 level, also kept constant throughout the runs, to 730 ppm, which approximates the average projection for the late twentyfirst century according to the SRES A2 scenario (Meehl et al. 2007). The A2 scenario assumes slow technological change and a large global population increase, and gives the largest CO_2 increase out of all the SRES scenarios included in CMIP3. The ΔSST_{GW} pattern is taken to be the CMIP3 MMEM change in SST between the periods 1980–1999 and 2080–2099. Figure 3 shows the November–April average of ΔSST_{GW} (with no added El Niño anomaly). The largest warming (>2.8 K) occurs over the equatorial eastern Pacific, near the east coast of central Africa, and over the tropical Atlantic. The least warming (<1.4 K) occurs in the south east of the domain. This warming pattern is reasonably robust, and has been found to be similar to the projections from the CMIP5 MMEM (Knutti et al. 2012).

All of the experiments conducted are summarised in Table 2.

4 Model response to increasing El Niño anomalies in the twentieth century/present climate

4.1 Precipitation response to El Niño

We begin our analysis by first investigating the effect of increasing the magnitude of the El Niño anomaly applied, with a background 20C SST climatology (i.e. the 20C runs described in Table 2). In Fig. 4, the panels show the 15-year November–April average precipitation in the tropics 35°S–35°N for $0 \leq \alpha \leq 4$. The top panel ($\alpha = 0$) corresponds to the 20C_0EN run, and the panels below this correspond to the 20C_[1EN–4EN] runs.

Moving down the panels of Fig. 4, as α is increased, two features stand out. Firstly, the precipitation increases dramatically near the equator between 160°E and 260°E, essentially along the ITCZ and equatorward side of the
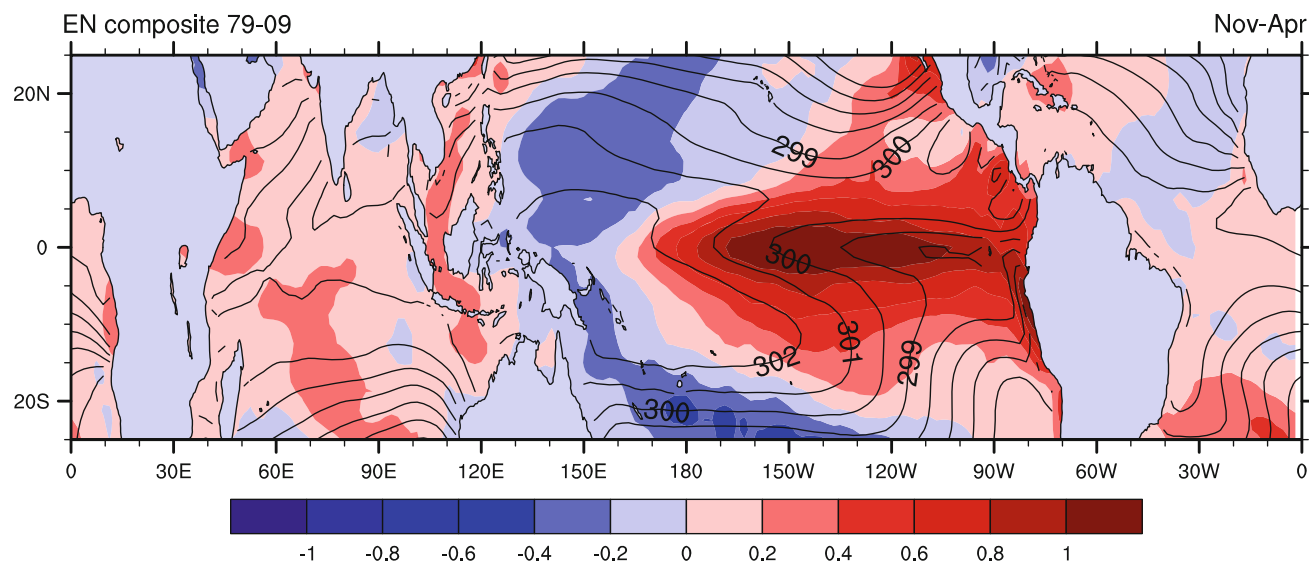
Fig. 2 SSTA$_{EN}$: *Shading* shows the composite of observed El Niño SST anomalies (November–April) from 1979 to 2009, with respect to the 1979–2009 climatology (shown as *contours*). Units are degrees Celsius
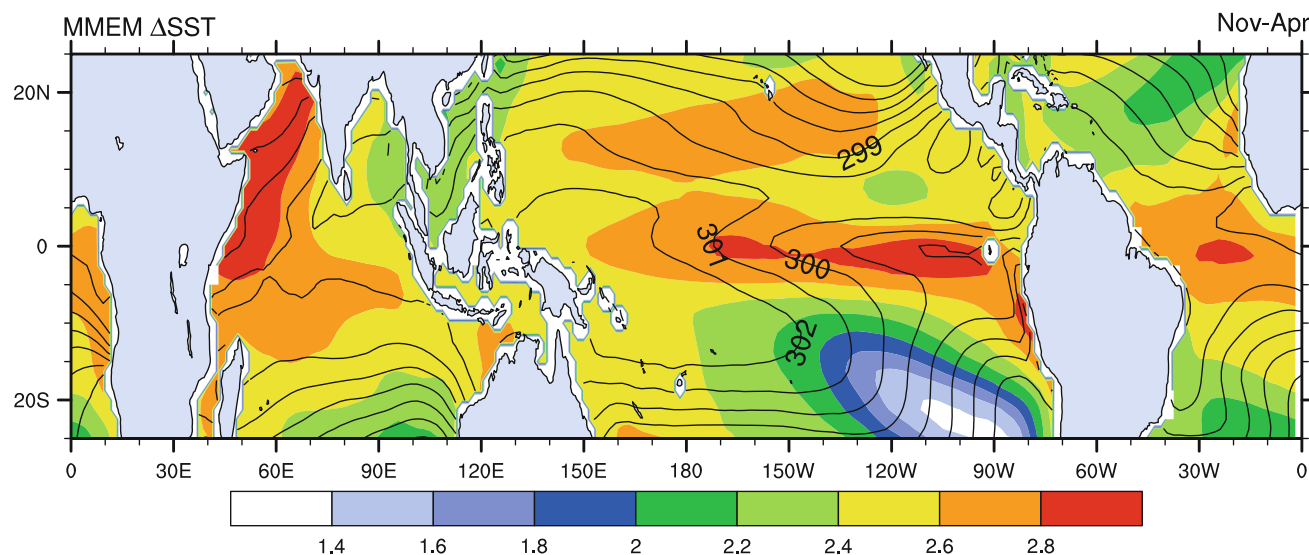

Fig. 3 ΔSST$_{GW}$: *Shading* shows the CMIP3 MMEM difference in SST between 1980–1999 and 2080–2099 (Nov–Apr), showing the only change in SST under the SRES A2 scenario. The twentieth century SST climatology is shown as *contours*. Units are degrees Celsius

SPCZ. The top panel shows that under weak ($\alpha = 1$) El Niño conditions, there is increased precipitation in the region 150°E–200°E, 10°S–5°N. This wet region is straddled by a dry band to the north and south west. Secondly, the precipitation pattern changes: the wetting/drying intensifies, the ITCZ shifts southwards and the centre of maximum precipitation, where the ITCZ and SPCZ merge, shifts eastwards from ~150°E to ~165°E (i.e. by ~1 km). A linear response would merely give a single pattern of change that becomes more intense as the magnitude of the imposed El Niño SST anomaly increases. Hence the eastward shift of the maximum precipitation

anomaly and the southward shift of the ITCZ are part of a nonlinear response.

We briefly compare Fig. 4 with Figs 13a and 14a of HKX01, which show December–March tropical precipitation anomalies for weak and strong El Niño composites (as defined in Sect. 1) respectively. In the weak El Niño case (Fig 13a, HKX01 and top panel, Fig. 4) both results show the increase in precipitation centred on 0°N, 180°E and the small decrease along the north-east part of South America. However the HKX01 results do not simulate the dry band between 5°N and 10°N. HKX01 also show increased precipitation over the north-west of South America

Table 2 Summary of ACCESS experiments described in this paper

Name	EN anomaly pattern multiplier α	Added ΔSST_{GW}	CO_2 levels (ppm)
20C_0EN (control)	0	N	346
20C_1EN	1	N	346
20C_2EN	2	N	346
20C_3EN	3	N	346
20C_4EN	4	N	346
21C_0EN	0	Y	730
21C_1EN	1	Y	730
21C_2EN	2	Y	730
21C_3EN	3	Y	730
21C_4EN	4	Y	730

From left to right, the columns show (i) the names of the runs, (ii) the multiplication factor α applied to the El Niño anomaly added to the climatological SSTs, (iii) whether the CMIP3 MMEM GW pattern was added to the SSTs, and (iv) which background CO_2 level was used

(i.e. around Peru), which is consistent with observations (see Fig. 1b), whereas we see no significant change in this region. In the strong El Niño case (Fig 14a, HKX01 and bottom panel, Fig. 4), the large increase in equatorial precipitation is seen in both results, as well as dry anomalies to the south west of the SPCZ and over the north-east of South America. However again, the HKX01 results do not simulate the dry band between 5 and 10°N. The HKX01 results show increased precipitation over parts of Peru (again, consistent with observations), whereas our results show drying over the entire northern part of South America and along the equatorial Atlantic.

Note that even though we have applied anomalies of up to α = 4, the model does not replicate the completely zonal SPCZ observed in the 82/83 and 97/98 events. In the bottom panel of Fig. 4, even though the SPCZ has shifted its orientation zonally, it still clearly has a diagonal component. This indicates that applying an SST anomaly with the spatial structure of $SSTA_{EN}$, even at large amplitudes, cannot fully reproduce zonal SPCZ events.

The top panel of Fig. 4 shows that for α = 0, there are two branches of SST_{max} in the central Pacific: just to the north of the maximum precipitation band of the SPCZ, and directly along the ITCZ. As α increases, both branches become more zonal until they merge along the equator between 150°E and 240°E. In all cases, the northern branch of SST_{max} lies directly over the ITCZ. However although the southern branch of SST_{max} lies close to the SPCZ, it is not positioned directly over areas of maximum precipitation. Thus even if the change in the orientation of the SPCZ is partially driven by SST_{max}, the exact location of precipitation patterns and their response to varying α must also

be affected by other mechanisms, such as the changing SST gradient between the SPCZ and equatorial cool tongue (Cai et al. 2012; Widlansky et al. 2013).

4.2 Role of circulation dynamics and thermodynamics in the response

In this section we calculate the moisture budget for each model run. To investigate the relative importance of dynamic (atmospheric circulation) and thermodynamic (atmospheric moisture) changes to the model responses, we calculate the breakdown of their respective contributions to the precipitation response.

We use a simplified version of the method employed by Seager et al. (2010) to approximate the moisture budget equation. Equations (4)–(7) of Seager et al. (2010) define the change in precipitation between two states to be

$$\delta P \approx \delta TH + \delta MCD + \delta COV + \delta E, \qquad (1)$$

where E is the evaporation, δTH is the thermodynamic component, δMCD is the component due to mean circulation dynamics, and δCOV is a co-varying term comprising transient eddy and surface terms. δTH and δMCD are defined to be

$$\delta TH = -1/(\rho g) \int_0^{p_s} \nabla \cdot (\mathbf{u}_0 [\delta q]) dp, \qquad (2)$$

$$\delta MCD = -1/(\rho g) \int_0^{p_s} \nabla \cdot ([\delta \mathbf{u}_0] q_0) dp, \qquad (3)$$

where ρ is the density of water, g is the acceleration due to gravity, p_s is the surface pressure, $\mathbf{u}$ is the horizontal wind vector, q is the specific humidity, and the subscript 0 denotes the values from the control run. We obtain P, E, $\mathbf{u}$, and q from model output, so are able to calculate the terms δE, δTH and δMCD directly. δCOV is not calculated directly but is defined to be the difference between δP and the sum of the other terms. Note that each of these terms can be broken down further into advective and divergent terms (Seager et al. 2010), however for the purposes of this study, we are only interested in their total amounts. In this calculation, we use the 15-year average of the November–April monthly means.

The top row of Fig. 5 shows the contribution of each of these terms to δP over the tropical Pacific for α = 1. From left to right, the columns show δP, δMCD, δTH, δE, and δCOV. These quantities are the anomalies for α = 1 calculated with respect to the α = 0 case.

It is clear that much of δP is dominated by the δMCD term, however, the other terms do contribute, to a lesser
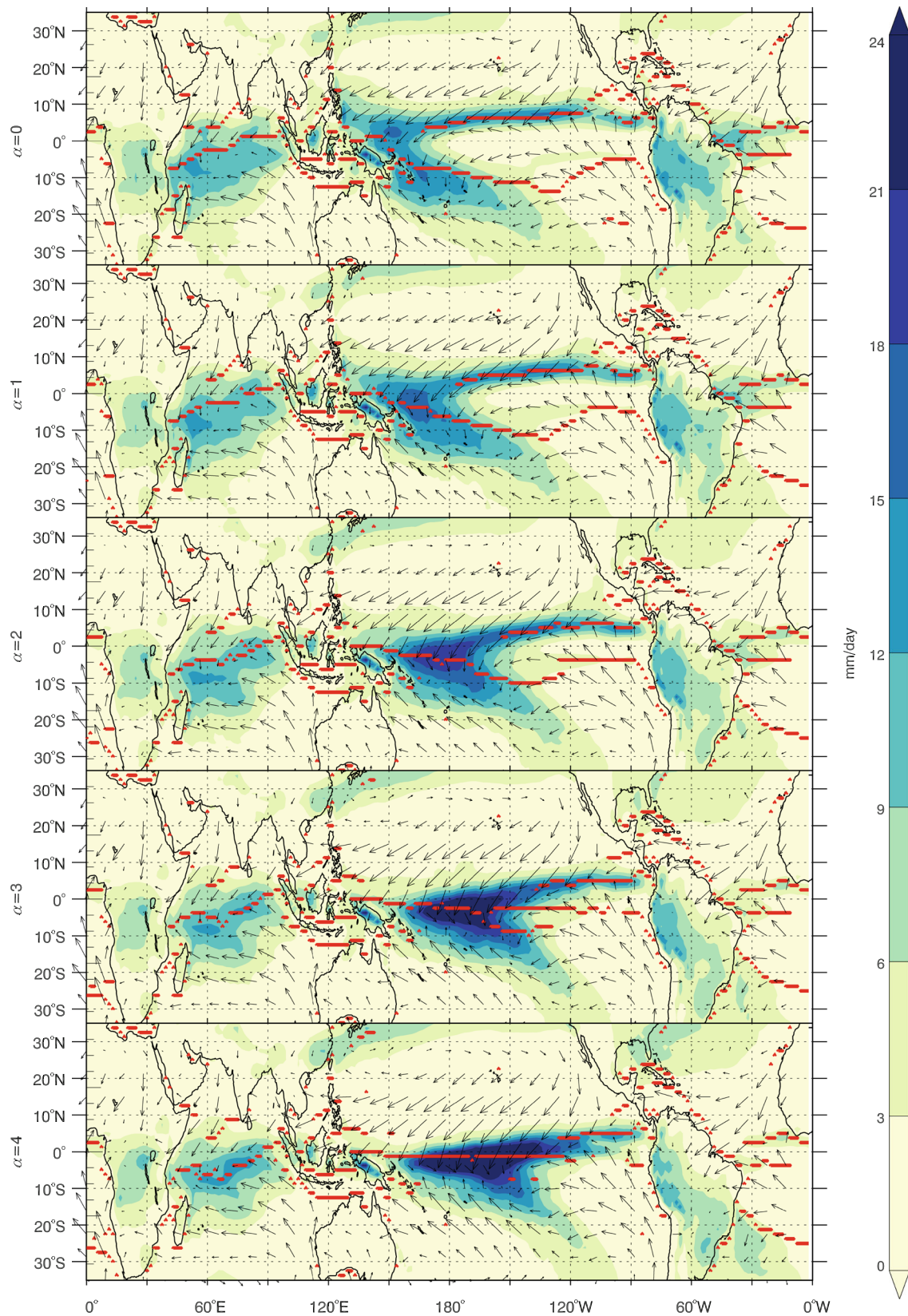
Fig. 4 Average 20C Nov–Apr precipitation P_0 (*shading*) and surface winds (*arrows*) from 15-year model integrations using annually-repeating 20C SST and CO_2 values (346 ppm). *Top to bottom* (i) $\alpha = 0$, (ii) $\alpha = 1$, (iii) $\alpha = 2$, (iv) $\alpha = 3$, and (v) $\alpha = 4$, where α is the El Niño anomaly pattern multiplier. The *thick red lines* indicate locations of local SST maxima

Fig. 5 *Linear response* In landscape mode, *top panel* 20C 15-year average Nov–Apr anomalies with respect to the $\alpha = 0$ run for preciptiation (δP) and its dynamic (δMCD), thermodynamic (δTH), evaporative (δE), and covariant (δCOV) contributions for $\alpha = 1$. *Nonlinear response* The *second* to *fourth* rows show the nonlinearities for δP(NL), δMCD(NL), δTH(NL), δE(NL), and δCOV(NL) terms. From *top* to *bottom*, rows correspond to (i) $\alpha = 2$, (ii) $\alpha = 3$, and (iii) $\alpha = 4$, where α is the El Niño anomaly pattern multiplier. Units are mm day
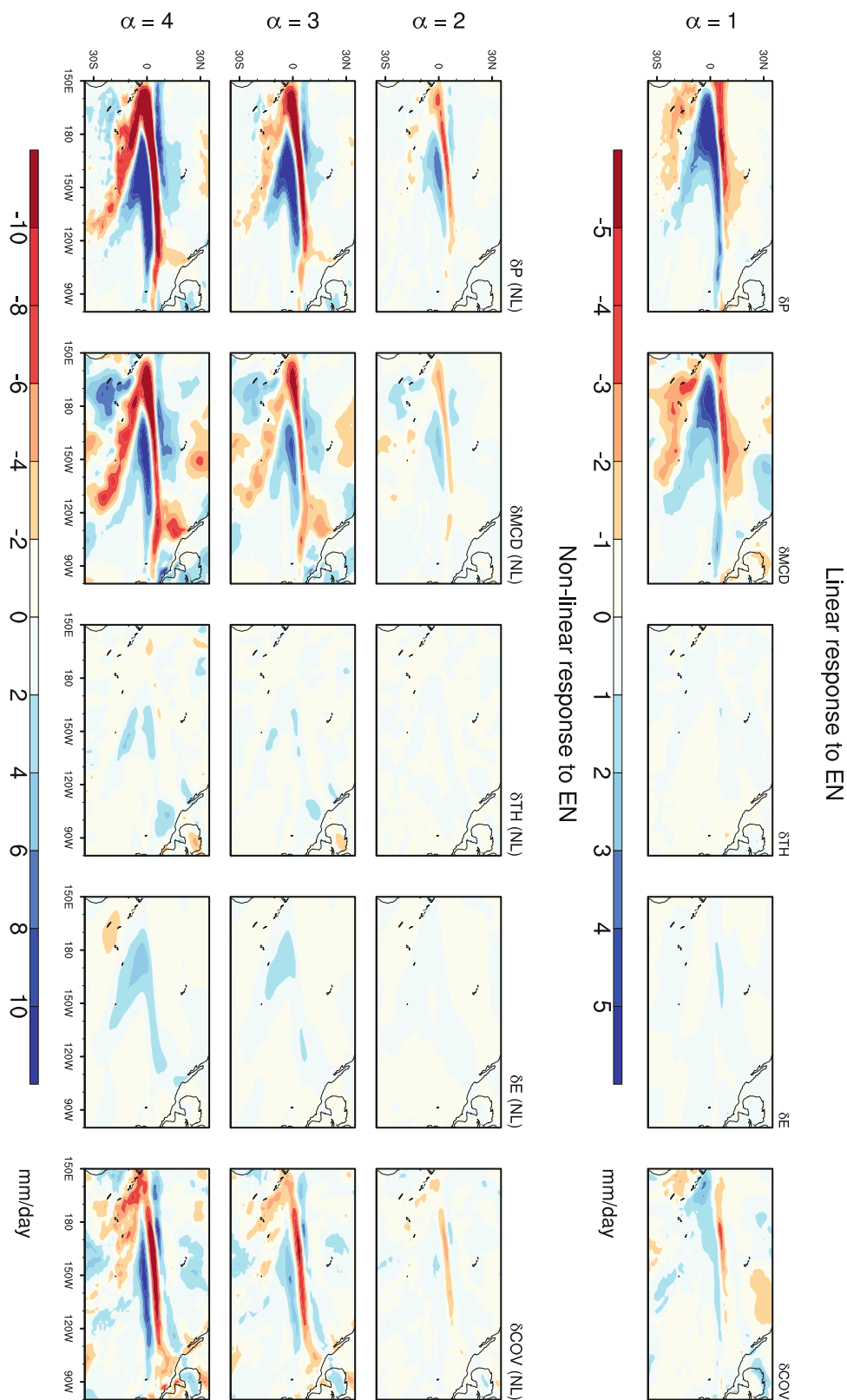
extent, in certain regions. Firstly, the drying along the south west SPCZ is due predominantly to δMCD, though its intensity is reduced by δCOV. The wetting along the ITCZ and north-east SPCZ is enhanced by δTH and δE, whereas the equatorwards shift of the ITCZ is linked to both δMCD and δCOV terms.
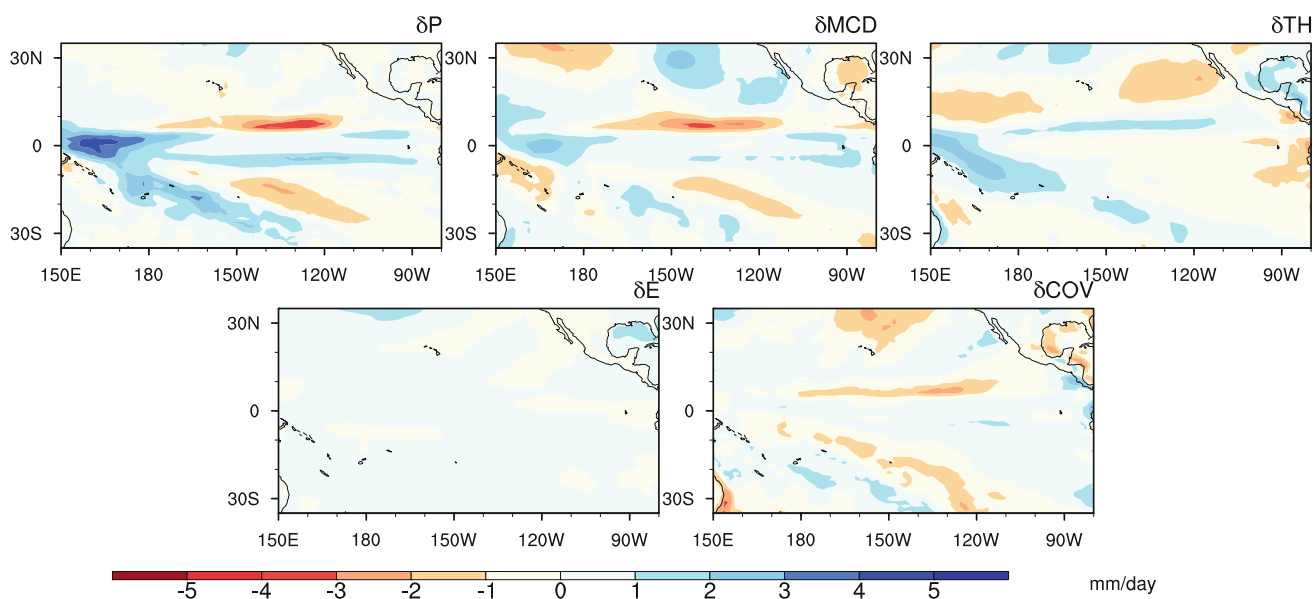
Fig. 6 Differences between the 20C and 21C climatological runs, where the global warming SST pattern ΔSST_{GW} is added and the CO_2 is increased to 730 ppm. The *panels* show 15-year average Nov–Apr changes in total precipitation P, and its breakdown into dynamic (MCD), thermodynamic (TH), evaporative (E), and covariant (COV) terms for $\alpha = 0$, where α is the El Niño anomaly pattern multiplier

4.3 Nonlinear response to strengthening El Niño

In Fig. 5, the second to fourth rows highlight the nonlinear response of the moisture budget terms in the Indo-Pacific region 120°E–280°E, 35°S–35°N to the increasing El Niño anomalies. From left to right, the columns show the nonlinearities in δP, δMCD, δTH, δE, and δCOV. We define the nonlinearity to be the difference between the $2 \leq \alpha \leq 4$ response and what the changes *would be* if the $\alpha = 1$ response was simply multiplied by α, e.g.

$$\delta P_\alpha(NL) = \delta P_\alpha - (\alpha \times \delta P_1), \tag{4}$$

where δP_α denotes the precipitation change with respect to the climatology for a given value of α, and δP_1 is the precipitation change for $\alpha = 1$. From top to bottom, rows 2–4 in Fig. 5 correspond to $\alpha = 2$, 3, and 4.

The structure and position of the nonlinearities are similar (though not identical) to that of the $\alpha = 1$ linear response (top row). Focusing on $\delta P_\alpha(NL)$, the most notable changes as α increases are the dramatically increased precipitation over the central-eastern equatorial Pacific, and the nonlinear drying over the south western part of the SPCZ. $\delta P_\alpha(NL)$ increases between 180° and 260°E and between 5°S and 5°N. This shows that the precipitation in this area increases more than expected from linearly extrapolating the $\alpha = 1$ pattern. Surrounding this region to the north and south west, $\delta P_\alpha(NL) < 0$. This nonlinear drying spans much of the ITCZ from 150°E–260°E and 0°N–10°N, and covers the south west of the SPCZ, extending to approximately 20°S. Note that having $\delta P_\alpha(NL) < 0$ does not necessarily mean that the overall precipitation decreases, but that the precipitation increases less than expected from a linear trend. For example, from Fig. 4, it is clear that the central eastern ITCZ gets wetter as α increases. However, Fig. 5 shows that the precipitation does not increase as much as it would if it followed a linear trend. Conversely, there are areas (such as the south west of the SPCZ) which experience a larger decrease in precipitation than expected from a linear trend.

As α increases, so does the contribution from each term, with little change in spatial structure in δTH, δE, and δCOV. However, the eastward expansion of the equatorial drying and maximum precipitation anomaly seen in δP is also apparent in δMCD, implying that this particular nonlinearity is driven primarily by changes in the winds. This is consistent with convergence on the equator and along the SPCZ moving eastwards and intensifying as α increases.

One interesting feature is that for $\alpha \geq 2$, $\delta P_\alpha(NL)$ is positive around 180°E, 5°N, indicating that this area dries less than predicted by a linear trend. In other words, the precipitation in the equatorial dry band does not decrease uniformly as α increases.

The structure, position, and intensity of $\delta MCD_\alpha(NL)$ are extremely similar to $\delta P_\alpha(NL)$ over the SPCZ and ITCZ. There is some nonlinear wetting over the north-east SPCZ due to the $\delta TH_\alpha(NL)$ and $\delta E_\alpha(NL)$ terms, though their contribution to the overall precipitation response is relatively small. The covariant term $\delta COV_\alpha(NL)$ displays a band of strong nonlinear drying along the equator, bounded to the north and south by bands of nonlinear wetting, enhancing the effects of $\delta MCD_\alpha(NL)$. It also contributes to the nonlinear drying over the south west SPCZ.

Fig. 7 In landscape mode, *left–right* 15-year average Nov–Apr changes in El Niño-driven anomalies in precipitation (δP), and its dynamic (δMCD), thermodynamic (δTH), evaporative (δE), and covariant (δCOV) terms, between the 20C and 21C runs, e.g. $\delta P(21C) - \delta P(20C)$. *Top–bottom* (i) $\alpha = 1$, (ii) $\alpha = 2$, (iii) $\alpha = 3$, and (iv) $\alpha = 4$, where α is the El Niño anomaly pattern multiplier
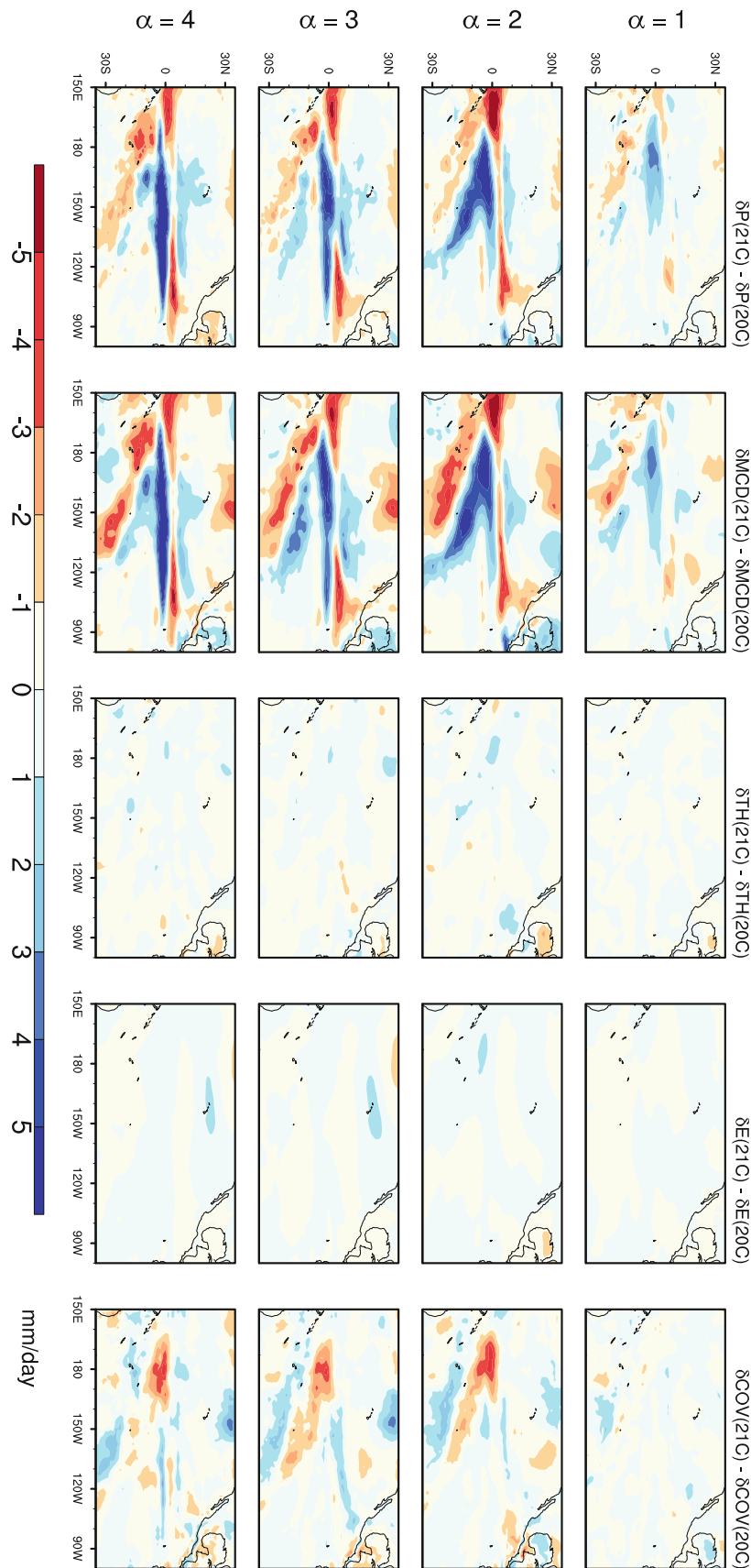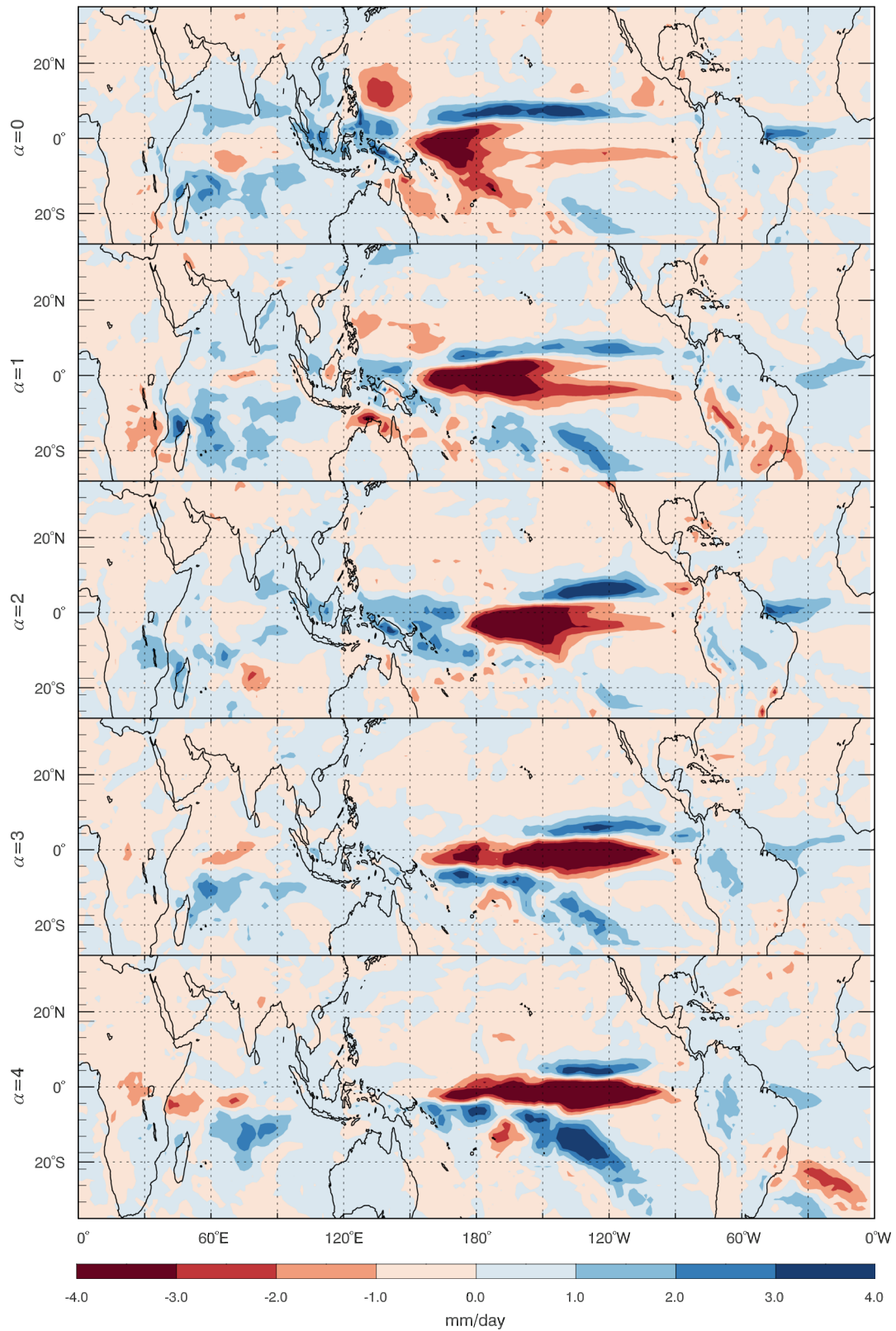
Fig. 8 Differences in the 15-year average Nov–Apr precipitation response to ΔSST_{GW} averaged over the tropical Pacific, and the full ΔSST_{GW} pattern (21C runs). *Top–bottom* (i) $\alpha = 0$, (ii) $\alpha = 1$, (iii) $\alpha = 2$, (iv) $\alpha = 3$, and (v) $\alpha = 4$, where α is the El Niño anomaly pattern multiplier

Fig. 9 Precipitation profiles along **a** the 219.4° longitude, from 25°S–25°N, and **b** the equator, from 140°E–300°E, for $0 \leq \alpha \leq 4$, where α is the El Niño SST anomaly pattern multiplier. The *solid lines* show the precipitation profiles for the 20C runs, and the *dashed contours* show the profiles for the 21C runs. The *shaded regions* in between highlight the change between the two experiments. The parts of the profiles corresponding to the SPCZ and ITCZ in (**a**) are marked in the figure
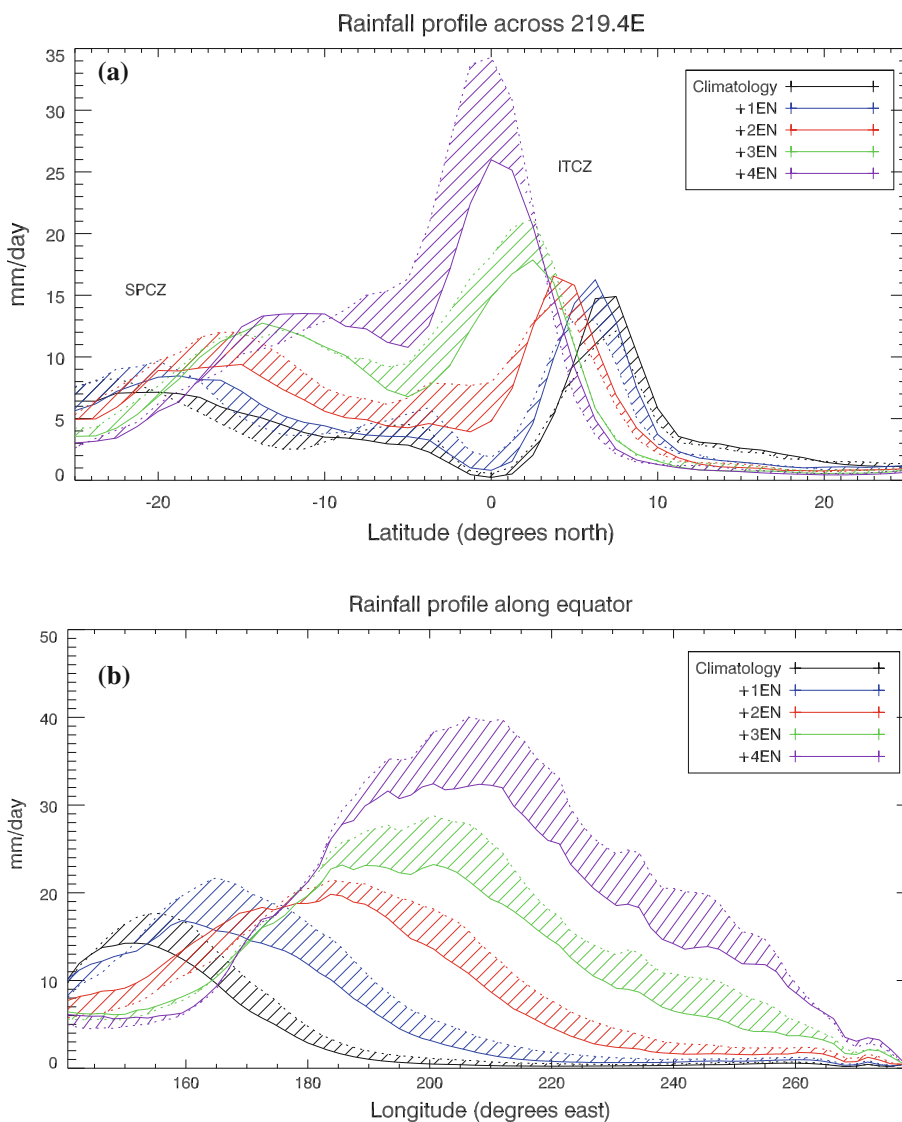
5 Impact of global warming

We now examine the model's response to global warming (run 21C). As detailed in Sect. 3, we add ΔSST_{GW}, the CMIP3 MMEM GW SST anomaly pattern, to the SSTs and increase the CO_2 levels from 346 to 730 ppm. The same five experiments are re-run, comprising a control run with climatological SSTs plus ΔSST_{GW}, and four runs with EN SST anomalies added, scaled by the factor α ranging between $1 \leq \alpha \leq 4$.

5.1 Precipitation response to global warming

We first discuss the precipitation response to ΔSST_{GW}. Figure 6 shows how the the precipitation and the moisture budget terms change in the 21C_0EN run, e.g. $P_{0,21C} - P_{0,20C}$. One general feature apparent is that there is significantly more precipitation in the equatorial Pacific,

except in the eastern Pacific where there is drying between 0°N and 10°N and between 210°E and 270°E in the 21C runs. The west ITCZ and west SPCZ become wetter compared with run 20C_0EN, whereas the east ITCZ and east SPCZ become drier.

5.2 Role of circulation dynamics and thermodynamics in the response

From left to right, the second to fifth panels in Fig. 6 show how the terms MCD, TH, E, and COV change in the 21C run. The dynamic term δMCD is the largest contributor to the drying along the north ITCZ and south east SPCZ, however, the thermodynamic term δTH also contributes significantly to the wetting along the equator and SPCZ. The covariant term plays a smaller role, but boosts the drying north of the ITCZ and in the south eastern tip of the SPCZ. The contribution from the evaporation term δE is

negligible. A similar analysis was performed by Brown et al. (2012b), who decomposed the CMIP5 MMEM change between 20C and 21C DJF climatological precipitation into dynamic, thermodynamic, and covariant components using the regime-sorting method of Emori and Brown (2005).

The balance between dynamic and thermodynamic responses is highly model dependent, as noted by Widlansky et al. (2013). Summing the contributions from the two responses from a multi-model ensemble yielded

a ±20% uncertainty for projections of moderate 1–2 °C tropical SST warming, and a ±30% uncertainty for stronger 2–3 °C warming (Widlansky et al. 2013). It should be noted therefore that our results are subject to our particular model biases. However, the dynamic and thermodynamic response to global warming from the $\alpha = 0$ case (Fig. 6) closely matches that of the CMIP5 MMEM (Brown et al. 2012b).

Although the impact of ΔSST_{GW} varies with α, it has several robust effects. Most importantly, it increases the

Fig. 10 Observed 1979–2009 Nov–Apr precipitation profiles along **a** the 218.75° longitude, from 25°S–25°N, and **b** 1.25°N, from 140°E–300°E, showing climatological (*black*), weak El Niño (*blue*), and strong El Niño (*red*) averages. *Solid lines* indicate GPCP observations, and *dashed lines* indicate CMAP observations
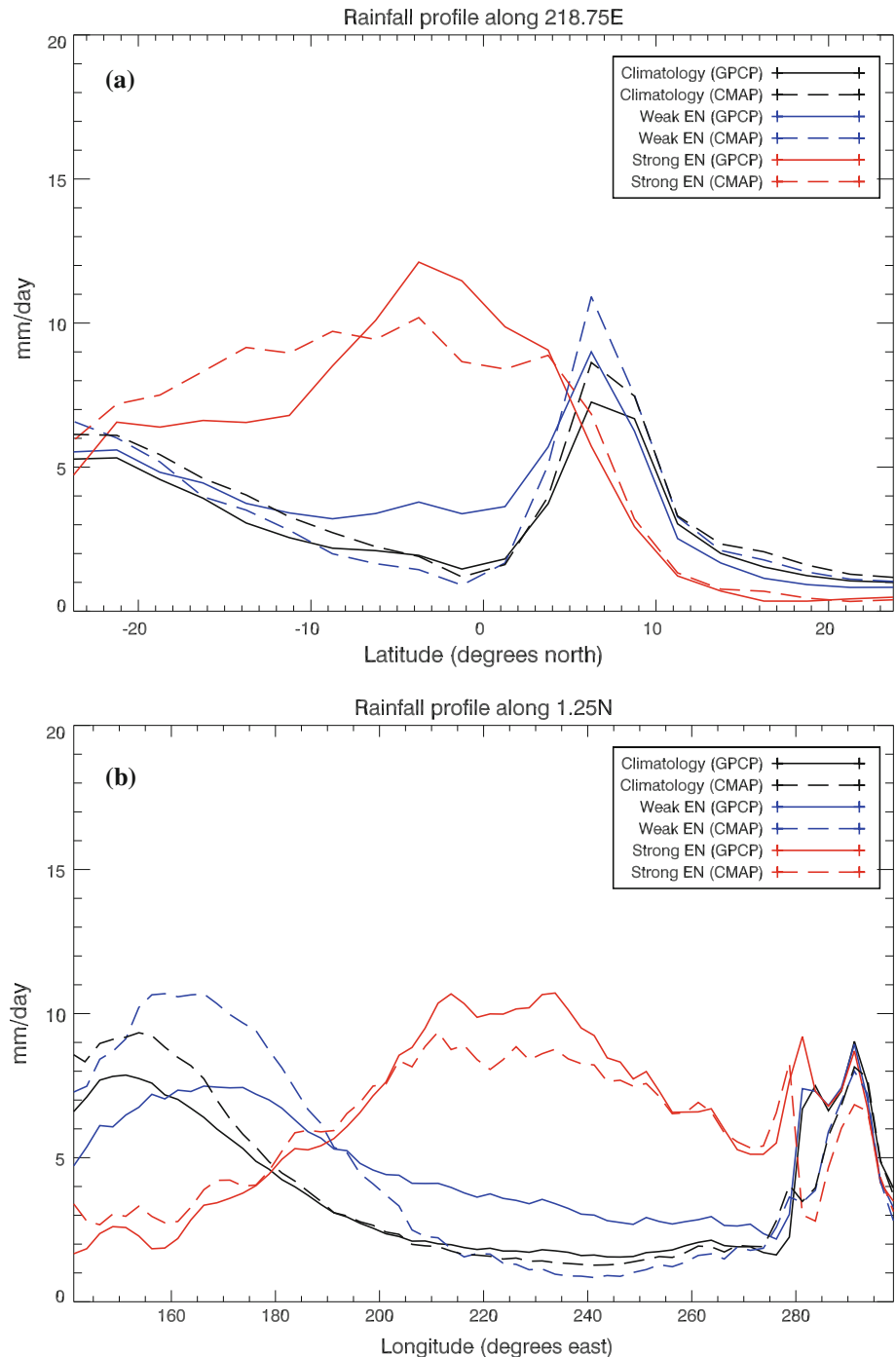
overall precipitation over the equatorial Pacific. It also causes the ITCZ to shift south towards the equator, and diminishes the south eastern tip of the SPCZ. These shifts are consistent with projections from CMIP3 coupled models (e.g. Australian Bureau of Meteorology and CSIRO 2011; Brown et al. 2012a).

5.3 Changes in response to El Niño due to global warming

How does the response to El Niño change under GW in our simulations? This question is addressed in Fig. 7, which compares the El Niño-driven ($\alpha \geq 1$) anomalies in the 20C and 21C runs. From left to right, the panels show the differences in 21C and 20C anomalies for P, MCD, TH, E, and COV, e.g. $\delta P(21C) - \delta P(20C)$. From top to bottom, the rows correspond to $\alpha = 1, 2, 3,$ and 4. Note that $\delta P_\alpha(21C)$ is the precipitation anomaly measured with respect to the 21C climatology ($\alpha = 0$), and $\delta P_\alpha(20C)$ is the anomaly measured with respect to the 20C climatology.

Focusing first on the precipitation response in the leftmost column, for $\alpha = 1$ (top panel), there is increased precipitation in the region where the ITCZ and SPCZ merge, in the region 5°S–5°N, 180°E–195°. For $\alpha = 2$ (second panel from top), the precipitation increase along the eastern band of the SPCZ is enhanced, whereas two other regions experience drying. Firstly, there is enhanced drying on the equator, to the west of the ITCZ/SPCZ. Secondly, there is some drying over the eastern part of the ITCZ. For $\alpha = 3$ and 4 (third from top and bottom panels), the enhanced wetting/drying patterns continue, but with the increased precipitation concentrated along the equator rather than over the SPCZ. For $\alpha = 4$, the area with the largest precipitation increase along the equator shifts from $\sim 180°$E in the 20C eastward to $\sim 240°$E in the 21C. The drying over the south western band of the SPCZ is also significantly increased. Note that the *structure* of the El Niño precipitation response also changes in the following ways: (i) the positive anomaly along the ITCZ shifts eastwards and equatorwards, and (ii) the negative anomaly along the western equatorial Pacific shifts eastwards, causing the western edge of the ITCZ to contract.

The changes in δP as α increases are dominated by changes in the dynamic component δMCD, as shown in Sect. 4. The next most important term is δCOV, which diminishes the effect of δMCD in the west ITCZ and the south west SPCZ, but adds to δMCD in the east ITCZ. The changes in δTH and δE are small compared to the other two terms.

In summary, Fig. 7 illustrates how the magnitude of the precipitation response to El Niño events under global warming is generally enhanced: regions which are prone to wetting will experience more intense wetting, and vice versa, in agreement with the coupled model study of Seager et al. (2012). Additionally, it suggests that the changes in the structure of the precipitation response with increasing EN strength, namely the equatorward shift of the ITCZ and the drying along the western edges of the ITCZ and SPCZ are also enhanced by global warming. Similar results were noted by Cai et al. (2012), who found that zonal SPCZ events are projected to increase under global warming.

5.4 Additional experiments

We also performed two sets of additional experiments to investigate the impact of increasing the CO_2 levels and adding ΔSST_{GW} individually. Firstly, in order to determine the effect of varying the CO_2 levels only, we ran a set of experiments identical to the 21C runs, but using 20C CO_2 values. We found that the amount and extent of the precipitation changes were small compared to the large-scale El Niño and global warming-driven changes. Thus the impact of global warming on Pacific precipitation is primarily determined by the SST changes associated with global warming.

Secondly, to determine the effect of the ΔSST_{GW} structure on the precipitation response, we also performed a set of experiments where we added uniform SST warming at each gridpoint in the tropical Pacific, i.e. ΔSST_{GW} averaged over 120°E–300°E, 25°S–25°N. Elsewhere, ΔSST_{GW} was applied unchanged. We used 21C CO_2 levels so the results could be compared directly to the 21C run. Figure 8 shows the difference between the precipitation response in the averaged ΔSST_{GW} run and the 21C run for all values of α. We found that while warmer SSTs generally increase the mean precipitation over the tropical Pacific, the detailed structure of the precipitation response is extremely sensitive to that of ΔSST_{GW}. When the spatially averaged ΔSST_{GW} is applied, there is less wetting over the central-eastern equatorial Pacific, and more wetting between 5° and 10°N and along the north-eastern part of the SPCZ. This is in agreement with previous studies of the precipitation response to different global warming SST patterns which show that the structure of ΔSST_{GW} strongly influences tropical precipitation patterns (Xie et al. 2010). This is an important point to note, as studies suggest greater inter-model confidence in the SST warming pattern compared to changes in precipitation (e.g. Xie et al. 2010).

6 Changes in the ITCZ and SPCZ

In Sects. 4 and 5 we described how the magnitude and structure of the tropical precipitation responds nonlinearly to increasing El Niño SST anomalies and how this changes
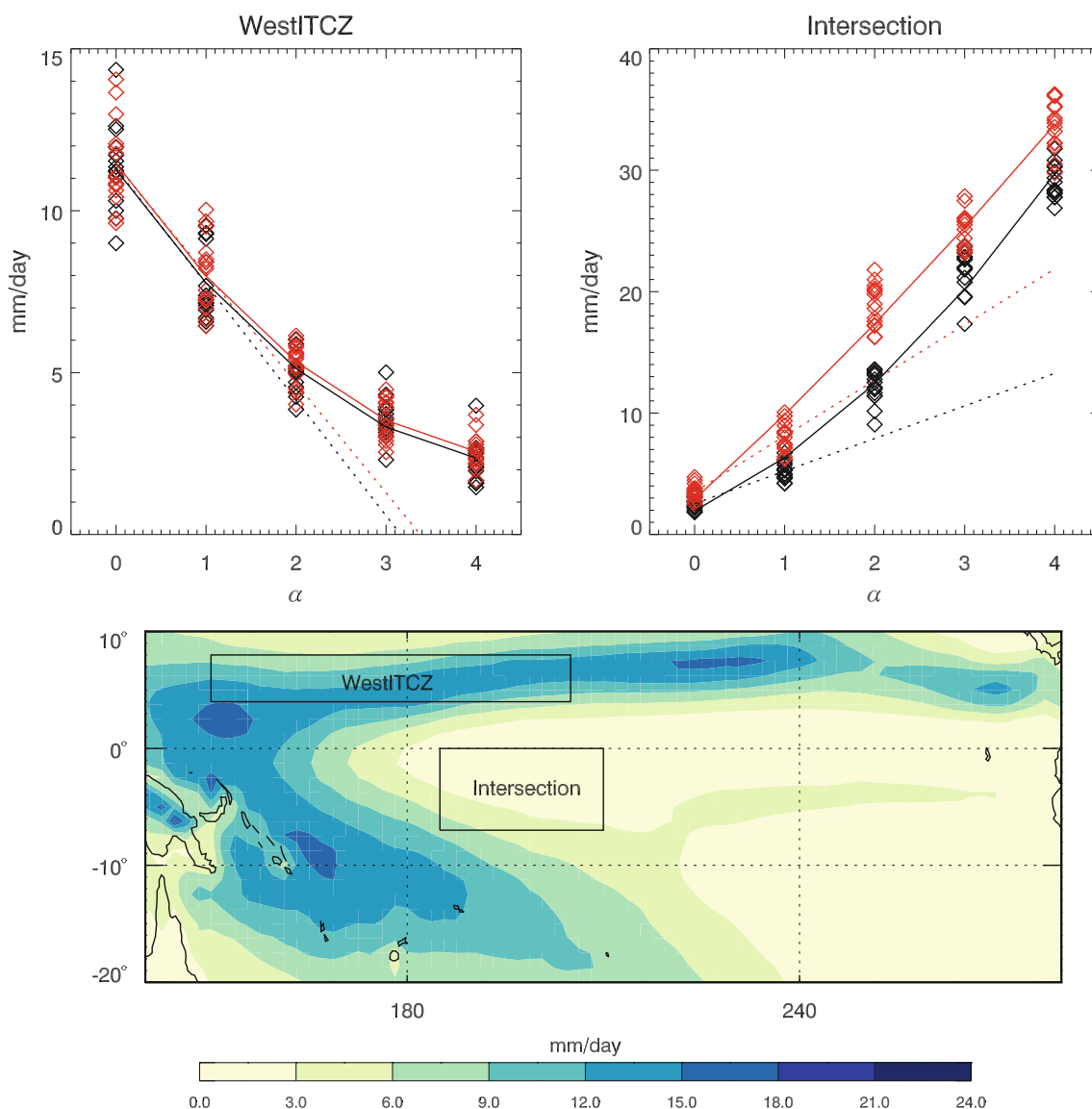
Fig. 11 *Top panels* precipitation averages for each individual model run for the 'West ITCZ' (*left panel*) and ITCZ/SPCZ 'Intersection' (*right panel*) regions, as a function of α, the El Niño SST anomaly pattern multiplier. *Black diamonds* correspond to the 20C run, *red diamonds* correspond to the 21C run. The *dashed contours* show the linear trend obtained by extrapolating the mean α = 1 precipitation change, and the *solid lines* show the best-fit polynomial to the *diamonds*. The nonlinear response to El Niño is highlighted by the departure of the *diamonds* from the *dashed line*. *Bottom panel* map showing the locations of the 'West ITCZ' and 'Intersection' boxes. *Shaded contours* show the climatological Nov–Apr precipitation

under global warming. In this section we provide more information on three major nonlinear changes: (i) the ITCZ shifts equatorwards and the SPCZ becomes more zonal, (ii) the maximum precipitation anomaly in the SPCZ and ITCZ shifts eastwards, and (iii) the total precipitation in the ITCZ and SPCZ increase nonlinearly. (i) The first nonlinearity is the equatorwards shift of the ITCZ and increased zonality of the SPCZ. We highlight this by plotting the precipitation profile along the 219.4°E longitude, between 25°S and 25°N. This longitude is chosen as it intersects both the ITCZ and SPCZ. Figure 9a shows the precipitation profiles

for $0 \leq \alpha \leq 4$, where α is the El Niño SST anomaly pattern multiplier as before, in different colours. The solid lines show the precipitation profiles for the 20C runs, and the dashed contours show the profiles for the 21C runs. The difference between the two experiments is hatched.

In all the runs, the SPCZ and ITCZ are clearly distinguishable and are marked in Fig. 9a. The SPCZ is located south of the equator, whereas the ITCZ occurs to the north. In the climatological (α = 0) runs (black curves), the ITCZ peaks around 8°N in both the 20C and 21C runs, although there is more precipitation in the 20C runs. As α increases,

the ITCZ peak moves gradually equatorwards and the 21C precipitation becomes larger than the 20C by $\alpha = 3$. For $\alpha = 4$, the ITCZ peaks at the equator in both cases, although in 21C it lies more towards the south of the equator than in 20C. The equatorward movement of the SPCZ as α increases is also apparent. For $\alpha = 0$, the SPCZ peaks at around 22°S in 20C and 23°S in 21C. The SPCZ peak shifts north as α increases; for $\alpha = 4$, the SPCZ peaks at around 15°S in the 20C and 8°S in the 21C, although there is no distinct peak in the 21C case.

(ii) The second nonlinearity is the eastwards shift of both the ITCZ and SPCZ. Figure 9b shows the precipitation profile along the equator, between 140°E and 300°E. As per Fig. 9a, the solid lines denote the 20C runs, the dashed contours denote the 21C runs, and the difference between the two experiments is hatched. For $\alpha = 0$, the precipitation peaks at approximately 150°E in the 20C and 155° in the 21C cases, where the ITCZ and SPCZ intersect. The peak moves eastwards as α increases, reaching approximately 205°E in 20C and 210° in 21C.

(iii) The total precipitation in both 20C and 21C runs increases nonlinearly as a function of α. However, the areas in which wetting and drying occur vary between the 20C and 21C cases. For example, in the 21C runs, there is more precipitation to the east of the region where the ITCZ and SPCZ intersect, but *less* precipitation to the west of this region.

Although our experiments are highly idealised and do not account for structural changes in $SSTA_{EN}$, we note that similar nonlinearities are observed in GPCP and CMAP data. Figure 10 shows the precipitation profiles along (a) 218.95°E, and (b) 1.25°N, the closest data points matching those in Fig. 9. The black lines show the 1979–2009 Nov–Apr climatological precipitation profiles, the red lines denote strong El Niño years (1982/1983 and 1997/1998), and the blue lines denote weak/moderate El Niño years (all other years; see Table 1). In Fig. 10a, the precipitation profile for weak El Niño years closely resembles the climatological profile, with a clear distinction between the ITCZ and SPCZ. During strong El Niño years, the ITCZ and SPCZ merge. In Fig. 10b, during weak El Niño years, the maximum precipitation over the western equatorial Pacific shifts eastwards by approximately 20° compared to climatology, whereas during strong El Niño years, the precipitation shifts eastwards dramatically by $\sim 70°$.

To further highlight the nonlinear precipitation changes in some regions, we choose two regions which clearly show nonlinear decreases/increases in precipitation. The first region, 'West ITCZ', spans 4°N–8°N, 150°E–205°E. The second region, 'Intersection', spans 7°S–0°, 185°E–210°E as it is where the ITCZ and SPCZ intersect for

$\alpha > 1$. In Fig. 11, the top two panels show the precipitation averages in these two regions as a function of α (black diamonds correspond to the 20C runs, and red diamonds correspond to the 21C runs), and the bottom panel shows the location of the regions in relation to the climatological precipitation patterns. The solid lines show the best-fit second order polynomial to the data, and dashed contours show the linear trend obtained by extrapolating the mean $\alpha = 1$ precipitation change. The 'West ITCZ' region (top left panel) experiences an overall drying as α increases. However for $\alpha \geq 2$ the drying is less severe than expected from the linear trend. The addition of the global warming SST pattern ΔSST_{GW} does not significantly affect the response in this region as it is slightly north of the equator, where most of the global warming-driven precipitation increase occurs. On the other hand, the 'Intersection' region (top right panel) experiences a dramatic (≥ 25 mm/day) precipitation increase in response to increasing α from 0 to 4. The 21C runs consistently produce more precipitation in all cases, though the increase is more pronounced for $\alpha \geq 2$. The response is nonlinear in both the 20C and 21C runs, with the linear response underestimating precipitation increases for $\alpha \geq 2$.

7 Summary and discussion

We performed sensitivity experiments using the atmospheric component of ACCESS to investigate (i) the effect of systematically increasing the magnitude of the El Niño SST anomaly on tropical precipitation, and (ii) the effect of global warming on the precipitation response to El Niño events.

As $SSTA_{EN}$ is increased, the total November–April precipitation in the ITCZ and SPCZ increases. The equatorial region where the ITCZ and SPCZ converge experiences a large nonlinear increase in precipitation, with the precipitation rate more than doubling during strong El Niño events, compared to the climatology. However, bands extending equatorially across the Pacific and along the south western flank of the SPCZ experience severe drying, resulting in the ITCZ shifting equatorwards, the SPCZ becoming more zonal, and the maximum precipitation anomaly along the ITCZ shifting eastwards by up to $\sim 10°$ longitude.

The results of these experiments demonstrate two key points: first, that the November–April precipitation across the Pacific responds nonlinearly to increasingly strong El Niño events. Second, the response to El Niño is enhanced in the presence of ΔSST_{GW} and an elevated CO_2 level. In the 21C runs, precipitation increases along the central and eastern equatorial Pacific but declines in the western Pacific between 0°N and 10°N.

We have shown that, in our model, global warming intensifies the nonlinear precipitation response to increasing El Niño SST anomalies in the tropical Pacific. However, the impact of ΔSST_{GW} on the precipitation changes varies as a function of El Niño magnitude. For example, ΔSST_{GW} tends to increase the precipitation along the equatorial Pacific, but its impact is greater during large El Niño events. During large El Niño events, the centre of the global warming-driven precipitation increase also shifts eastwards. Global warming also increases precipitation in the climatological position of the SPCZ, but reduces precipitation in the south eastern tip of the SPCZ for all α. However, as noted in Sect. 5.4, these results are highly dependent on the spatial pattern of ΔSST_{GW}, as well as being model-dependent.

Breaking down the precipitation response into dynamic, thermodynamic, evaporative, and covariant terms, we find that the response to increasing $SSTA_{EN}$ is dominated by changes in the atmospheric circulation. Along the ITCZ, changes in the covariance term, which includes a transient eddy term, daily surface fluxes (and errors in our method), also enhance the response to increasing α. The thermodynamic and evaporative terms do not contribute significantly to the precipitation response. The precipitation response to global warming is also strongly influenced by changes to the atmospheric circulation, although there is also a comparable contribution to the precipitation increase from the thermodynamic component.

We also showed that the spatial structure in ΔSST_{GW} strongly influences both precipitation and nonlinearity of the precipitation response to El Niño, as well as that of $SSTA_{EN}$. Experiments performed using a spatially uniform ΔSST_{GW} pattern in the Pacific yield significantly different results from those using the full ΔSST_{GW} pattern; in particular the precipitation along the central-eastern Pacific decreases and the precipitation along the north-eastern ITCZ increases. The importance of changes in the background SST on the precipitation response to ENSO was also noted by Cai et al. (2012), who found an increase in the frequency of zonal SPCZ events in some CMIP3 models, even though the amplitude of El Niño events in the models remained unchanged.

Studies of 21C projections under the SRES A2 scenario from the CMIP3 models show that precipitation in both the ITCZ and SPCZ is projected to increase (Brown et al. 2012a; Australian Bureau of Meteorology and CSIRO 2011). Brown et al. (2012a) analysed the projected changes in the SPCZ. The authors found that 11 out of 16 chosen CMIP3 models predict an increase in mean DJF precipitation in the SPCZ and a contraction of the eastern edge of the SPCZ, although the multi-model mean shows no shift in orientation. Under El Niño conditions, the multi-model mean SPCZ is projected to become more zonal in the 21C (Brown et al. 2012a). This is consistent with our results.

Note however that a direct comparison of the SPCZ behaviour from our SST-forced AGCM experiments to that of the coupled CMIP3 models is difficult, as the CMIP3 models produce an SPCZ that is too zonal (Brown et al. 2012a), whereas our AGCM experiments produce an SPCZ which more closely matches the observations. More recently, Widlansky et al. (2013) performed experiments using a combination of SST-forced and coupled climate models to provide a clearer projection of SPCZ behaviour under future greenhouse warming. The authors found that the balance between dynamic and thermodynamic responses to warming SSTs is model dependent, however the MMEM indicates that the SPCZ dries under moderate tropical SST warming (1–2 °C) and becomes wetter under stronger tropical warming (>3 °C).

In this study we have exploited the fact that there is no consensus yet on whether the spatial pattern associated with El Niño or the magnitude of events will change under global warming. We adopted the working 'null' hypothesis that no changes to the structure of the magnitude of El Niño SST anomalies under global warming will occur. Thus we have obtained estimates of the precipitation response to El Niño in the twentyfirst century, assuming the spatial structure and magnitude of El Niño SST anomalies do not change under global warming.

We also used a single SST anomaly pattern for El Niño ($SSTA_{EN}$). Allowance was made to increase the magnitude of the anomalies by multiplying this pattern by a number α = 1, 2, 3, 4. $SSTA_{EN}$ used here is based on a composite of El Niño events between 1979 and 2009, and includes both CT and WP events. Hence the results presented here do not address issues related to differences in SST anomalies between such classes. Additionally, by using annually-repeating SSTs and analysing the average November–April precipitation, we do not consider the time evolution of the El Niño events. Lengaigne (2009) showed that the strong El Niño events of 1982/1983 and 1997/1998 evolved differently compared to weak El Niño events, in particular the warm SST anomalies over the eastern equatorial Pacific persisted several months longer. Nor have we addressed the impact of global warming on precipitation during La Niña events.

Finally note that our results indicate that the nonlinearity of the precipitation response to increasing α alone increases the zonality of the SPCZ. However it does not fully reproduce the near-zonal SPCZ evident during the large El Niño years of 1982/1983 and 1997/1998 (Vincent et al. 2011; Cai et al. 2012). We expect to address this issue, as well as the impact of the spatial structure of ΔSST_{GW}, more fully in future work.

References

Adler RF, Huffman GJ, Chang A, Ferraro R, Xie P, Janowiak J, Rudolf B, Schneider U, Curtis S, Bolvin D, Gruber A, Susskind J, Arkin P, Nelkin E (2003) The Version 2 Global Precipitation Climatology Project (GPCP) monthly precipitation analysis (1979–present). J Hydrometeorol 4:1147–1167

Australian Bureau of Meteorology and CSIRO (2011) Climate change in the Pacific: scientific assessment and new research. Volume 1: regional overview. Volume 2: Country Reports

Bi D, Dix M, Marsland S, OFarrell S, Rashid HA, Uotila P, Hirst T, Kowalczyk E, Golebiewski M, Sullivan A, Yan H, Hanna N, Franklin C, Sun Z, Vohralik P, Watterson I, Zhou X, Fiedler R, Collier M, Ma Y, Noonan J, Stevens L, Uhe P, Zhu H, Hill R, Harris C, Griffies S, Puri K (2012) The ACCESS coupled model: description, control climate and preliminary validation. Aust Meteorol Oceanogr J, submitted

Bradley R, Diaz HF, en Eischeid JK (1987) ENSO signal in continental precipitation records. Nature 327:497–501

Brown JR, Power SB, Delage FP, Colman RA, Moise AF, Murphy BF (2011) Evaluation of the South Pacific Convergence Zone in IPCC AR4 climate model simulations of the twentieth century. J Clim 24:1565–1582

Brown JR, Moise A, Delage F (2012a) Changes in the South Pacific Convergence Zone in IPCC AR4 future climate projections. Clim Dyn 39:1–19. doi:10.1007/s00382-011-1192-0

Brown JR, Moise A, Colman RA (2012b) The South Pacific Convergence Zone in CMIP5 simulations of historical and future climate. Clim Dyn. doi:10.1007/s00382-012-1591-x

Cai W, van Rensch P, Cowan T, Sullivan A (2010) Asymmetry in ENSO teleconnection with regional rainfall, its multidecadal variability, and impact. J Clim 23:4944–4955

Cai W, Lengaigne M, Borlace S, Collins M, Cowan T, McPhaden M, A T, Power S, Brown J, Menkes C, Ngari A, Vincent E, Widlansky M (2012) More extreme swings of the South Pacific Convergence Zone due to greenhouse warming. Nature 488:365–369

Chiang JC, Kushnir Y, Zebiak SE (2000) Interdecadal changes in eastern Pacific ITCZ variability and its influence on the Atlantic ITCZ. Geo Res Lett 27:3687–3690

Collins M, An SI, Cai W, Ganachaud A, Guilyardi E, Jin FF, Jochum M, Lengaigne M, Power S, Timmermann A, Vecchi G, Wittenberg A (2010) The impact of global warming on the Tropical Pacific Ocean and El Niño. Nat Geosci 3:391–397

Cusack S, Edwards JM, Crowther JM (1999) Investigating k distribution methods for parameterizing gaseous absorption in the Hadley Centre Climate Model. J Geogr Res 104(D2):2051–2057

Davies T, Cullen MJP, Malcolm AJ, Mawson MH, Staniforth A, White AA, Wood N (2005) A new dynamical core for the Met Office's global and regional modelling of the atmosphere. Q J R Meteorol Soc 131(608):1759–1782. doi:10.1256/qj.04.101

Edwards JM, Slingo A (1996) Studies with a flexible new radiation code. I: choosing a configuration for a large-scale model. Q J R Meteorol Soc 122(531):689–719. doi:10.1002/qj.49712253107

Emori S, Brown SJ (2005) Dynamic and thermodynamic changes in mean and extreme precipitation under changed climate. Geophys Res Lett 32:L17706. doi:10.1029/2005GL023272

Essery R, Best M, Cox P (2001) MOSES 2.2 technical documentation. Hadley Centre Technical Note 30, Met Office, Exeter, United Kingdom. http://www.metoffice.gov.uk/research/hadley centre/pubs/HCTN/index.html

Fritsch J, Chappell C (1980) Numerical prediction of convectively driven mesoscale pressure systems. Part I: convective parameterization. J Atmos Sci 37:1722–1733

Folland CK, Renwick JA, Salinger MJ, Mullan AB (2013) Relative influences of the Interdecadal Pacific Oscillation and ENSO on the South Pacific Convergence Zone. Geophys Res Lett 29(13). doi:10.1029/2001GL014201

Gregory D, Rowntree PR (1990) A mass flux convection scheme with representation of cloud ensemble characteristics and stability-dependent closure. Mon Weather Rev 118:1483–1506

Gregory D, Inness P, Gregory J (1999) Convection Scheme. In: Unified Model Documentation Paper 27, Met Office, Exeter, United Kingdom

Hoerling MP, Kumar A, Zhong M (1997) El Niño, La Niña, and the nonlinearity of their teleconnections. J Clim 10:1769–1786

Hoerling MP, Kumar A, Xu TY (2001) Robustness of the nonlinear climate response to ENSO's extreme phases. J Clim 14:1277–1293

Huffman GJ, Adler RF, Bolvin DT, Gu G (2009) Improving the global precipitation record: GPCP version 2.1. Geophys Res Lett 36:L17,808. doi:10.1029/2009GL040000

Hurrell JW, Hack JH, Shea D, M CJ, Rosinski J (2008) A new sea surface temperature and sea ice boundary dataset for the community atmosphere model. J Clim 21:5145–5153. doi:10.1175/2008JCLI2292.1

Knutti R, Sedláček J (2012) Robustness and uncertainties in the new CMIP5 climate model projections. Nat Clim Change 3:369–373

Kug JS, Jin FF, An SI (2009) Two types of El Niño events: cold tongue El Niño and warm pool El Niño. J Clim 22:1499–1515

Lau KM, Boyle JS (1987) Tropical and extratropical forcing of the large-scale circulation: a diagnostic study. Mon Weather Rev 115:400–28

Lengaigne M, Vecchi GA (2009) Contrasting the termination of moderate and extreme El Niño events in coupled general circulation models. Clim Dyn. doi:10.1007/s00382-009-0562-3

Lock AP, Brown AR, Bush MR, Martin GM, Smith RNB (2000) A new boundary layer mixing scheme. Part I: scheme description and single-column model tests. Mon Weather Rev 128:3187–3199

Martin GM, Ringer MA, Pope VD, Jones A, Dearden C, Hinton TJ (2006) The physical properties of the atmosphere in the New Hadley Centre Global Environmental Model (HadGEM1). Part I: model description and global climatology. J Clim 19:1274–1301

Martin GM, Milton SF, Senior CA, Brooks ME, Ineson S (2010) Analysis and reduction of systematic errors through a seamless approach to modeling weather and climate. J Clim 23:5933–5957

Martin GM, Bellouin N, Collins WJ, Culverwell ID, Halloran PR, Hardiman SC, Hinton TJ, Jones CD, McDonald RE, McLaren AJ, O'Connor FM, Roberts MJ, Rodriguez JM, Woodward S, Best MJ, Brooks ME, Brown AR, Butchart N, Dearden C, Derbyshire SH, Dharssi I, Doutriaux-Boucher M, Edwards JM,

Falloon PD, Gedney N, Gray LJ, Hewitt HT, Hobson M, Huddleston MR, Hughes J, Ineson S, Ingram WJ, James PM, Johns TC, Johnson CE, Jones A, Jones CP, Joshi MM, Keen AB, Liddicoat S, Lock AP, Maidens AV, Manners JC, Milton SF, Rae JGL, Ridley JK, Sellar A, Senior CA, Totterdell IJ, Verhoef A, Vidale PL, Wiltshire A (2011) The HadGEM2 family of Met Office Unified Model Climate configurations. Geosci Model Dev Discuss 4(2):765–841. doi:10.5194/gmdd-4-765-2011

McGregor S, Timmermann A, Schneider N (2012) The effect of the South Pacific Convergence Zone on the termination of El Nio events and the meridional asymmetry of ENSO. J Clim 25:5566–5586

McGregor S, Ramesh N, Spence P, England MH, McPhaden MJ, Santoso A (2013) Meridional movement of wind anomalies during ENSO events and their role in event termination. Geophys Res Lett 40:749–754

McPhaden MJ, Lee T, McClurg D (2011) El Niño and its relationship to changing background conditions in the Tropical Pacific. Geophys Res Lett 38:15709. doi:10.1029/2011GL048275

Meehl G, TF Stocker W, Collins P, Friedlingstein A, Gaye J, Gregory A, Kitoh R, Knutti J, Murphy A, Noda S, Raper I, Watterson A, Weaver, Zhao ZC (2007) Global climate projections. In: Climate change 2007: the physical science basis. Contribution of Working Group I to the Fourth Assessment Report of the Intergovernmental Panel on Climate Change. Cambridge University Press, Cambridge, United Kingdom and New York, NY, USA

Meehl GA (1987) The annual cycle and interannual variability in the Tropical Pacific and Indian Ocean Regions. Mon Weather Rev 115:27–50. doi:10.1175/1520-0493(1987)115<0027:TACAIV>2.0.CO;2

Monahan AH, Dai A (2004) The spatial and temporal structure of ENSO nonlinearity. J Clim 17(15):3026–3036. doi:10.1175/1520-0442(2004)017%3C3026:TSATSO%3E2.0.CO;2

Mullan AB (1996) Non-linear effects of the southern oscillation in the New Zealand region. Aust Meteorol Mag 45:83–99

Münnich M, Neelin JD (2005) Seasonal influence of ENSO on the Atlantic ITCZ and equatorial South America. Geophys Res Lett 32:L21,709

Newman M, Shin SI, Alexander MA (2011) Natural variation in ENSO flavors. Geophys Res Lett L14705. doi:10.1029/2011GL047658

Ohba M, Ueda H (2009) Role of nonlinear atmospheric response to SST on the asymmetric transition process of ENSO. J Clim 22:177–192

Okumura YM, Deser C (2010) Asymmetry in the duration of El Niño and La Niña. J Clim 23:5826–5843

Philander S (1990) El Niño, La Niña, and the Southern Oscillation. Academic Press, New York

Power S, Smith IN (2007) Weakening of the Walker Circulation and apparent dominance of El Niño both reach record levels, but has ENSO really changed? Geophys Res Lett 34:L18,702,4

Power S, Haylock M, Colman R, Wang X (2006) The predictability of interdecadal changes in ENSO and ENSO teleconnections. J Clim 19:4755–4771

Ropelewski CF, Halpert MS (1989) Precipitation patterns associated with the high index phase of the Southern Oscillation. J Clim 2:268–284. doi:10.1175/1520-0442(1989)002<0268:PPAWTH>2.0.CO;2

Seager R, Naik N, Vecchi GA (2010) Thermodynamic and dynamic mechanisms for large-scale changes in the hydrological cycle in response to global warming. J Clim 23:4651–4668. doi:10.1175/2010JCLI3655.1

Seager R, Naik N, Vogel L (2012) Does global warming cause intensified interannual hydroclimate variability? J Clim 25:3355–3372. doi:10.1175/JCLI-D-11-00363.1

Smith RNB (1990) A scheme for predicting layer clouds and their water content in a general circulation model. Q J R Meteorol Soc 116:435–460

Smith RNB (1993) Experience and developments with the layer cloud and boundary layer mixing schemes in the UK Meteorological Office Unified Model. In: Proceedings of ECMWF/GCSS workshop on parametrization of the cloud-topped boundary layer, ECMWF, Reading, England, pp 319–339

Staniforth A, White A, Wood N (2003) Analysis of semi-Lagrangian trajectory computations. Q J R Meteorol Soc 129(591):2065–2085. doi:10.1256/qj.02.115

Streten NA (1973) Some characteristics of satellite-observed bands of persistent cloudiness over the Southern Hemisphere. Mon Weather Rev 101:486–495. doi:10.1175/1520-0493(1973)101<0486:SCOSBO>2.3.CO;2

Trenberth KE (1976) Spatial and temporal variations of the Southern Oscillation. Q J R Meteorol Soc 102(433):639–653. doi:10.1002/qj.49710243310, http://dx.doi.org/10.1002/qj.49710243310

Vecchi GA, Wittenberg AT (2010) El Niño and our future climate: where do we stand? Wiley Interdiscip Rev Clim Change 1:260–270

Vincent DG (1994) The South Pacific Convergence Zone (SPCZ): a review. Mon Weather Rev 122:1949–1970

Vincent E, Lengaigne M, Menkes C, Jourdain N, Marchesiello P, Madec G (2011) Interannual variability of the South Pacific Convergence Zone and implications for tropical cyclone genesis. Clim Dyn 36:1881–1896. doi:10.1007/s00382-009-0716-3

Waliser DE, Gautier C (1993) A satellite-derived climatology of the ITCZ. J Clim 6:2162–2174

Widlansky MJ, Webster PJ, Hoyos CD (2011) On the location and orientation of the South Pacific convergence zone. Clim Dyn 36:561–578

Widlansky MJ, Timmermann A, Stein K, McGregor S, Schneider N, England MH, Lengaigne M, Cai W (2013) Changes in South Pacific rainfall bands in a warming climate. Nat Clim Change 3:417–423

Wilson DR, Ballard SP (1999) A microphysically based precipitation scheme for the UK meteorological office unified model. Q J R Meteorol Soc 125(557):1607–1636. doi:10.1002/qj.49712555707

Wu B, Li T, Zhou T (2010) Asymmetry of atmospheric circulation anomalies over the western North Pacific between El Niño and La Niña. J Clim 23:4807–4822

Xie SP, Deser C, Vecchi GA, Ma J, Teng H, Wittenberg AT (2010) Global warming pattern formation: sea surface temperature and rainfall. J Clim 23:966–986

Yeh SW, Kug JS, Dewitte B, Kwon MH, Kirtman BP, Jin FF (2009) El Niño in a changing climate. Nature 461:511–514